Supporting Information

Engineering Annular Donor-Acceptor Reaction Chamber with Spontaneous Feedstock Collection for Boosting CO_2 Photoreduction

Zhanpeng Zhou [a,b], Hao Zeng [a], Chengyang Feng [c,*], Ling Li [a,b], Rongdi Tang [a,d], Wenbo Li [a,b], Ying Huang [b,*], Yaocheng Deng [a,*]

[a] College of Environment & Ecology, Hunan Agricultural University, Changsha 410128, China;

[b] College of Resources, Hunan Agricultural University, Changsha 410128, China;

[c] KAUST Catalysis Center, Physical Sciences and Engineering Division, King Abdullah University of Science and Technology, Thuwal 23955-6900, Saudi Arabia;

[d] College of Environmental Science and Engineering, Hunan University and Key Laboratory of Environmental Biology and Pollution Control (Hunan University), Ministry of Education, Changsha 410082, P. R. China.

Table of contents

Supplementary Text S1. Experimental section

Synthesis of bulk g-C_3N_4.

Firstly, 10 g of urea were finely ground using an agate mortar and transferred to a 100 mL ceramic crucible. The ceramic crucible was hermetically sealed with tin foil and covered, before being placed in a muffle furnace. The temperature was gradually increased to 550 °C at a rate of 5 °C/min under an air atmosphere, and subsequently maintained at this temperature for a duration of 2 h. After cooling, the solid obtained in the crucible is thoroughly pulverized and transferred into a porcelain boat. Subsequently, the uncovered porcelain boat is positioned inside a tube furnace and subjected to a N_2 atmosphere while gradually heating at a rate of 5 °C/min until reaching 500 °C for 2 h. The obtained products are denoted as BCN.

Synthesis of methylated and phosphorus doped g-C_3N_4.

The first step is to thoroughly grind 10 g of urea using an agate mortar. Subsequently, x mg (x = 5~30) of Na_2HPO_4 and y mg (y = 20~50) of acetamide are added to the ground urea powder, followed by gentle mixing. The mixture undergoes the identical two-step heating procedure as that of the BCN synthesis process. The obtained products are denoted as NPxEAy (x represents the amount of Na_2HPO_4 added, and y represents the amount of acetamide added), with the best performance referred to as NPEA.

Synthesis of phosphorus doped g-C_3N_4.

The first step is to thoroughly grind 10 g of urea using an agate mortar. Subsequently, x mg (x = 5~30) of Na_2HPO_4 were added to the ground urea powder, followed by gentle mixing. The mixture undergoes the identical two-step heating procedure as that of the BCN synthesis process. The obtained products are denoted as NPx (x represents the amount of Na_2HPO_4 added), with the best performance referred to as NPCN.

Synthesis of methylated g-C_3N_4.

The first step is to thoroughly grind 10 g of urea using an agate mortar. Subsequently, y mg (y = 20~50) of acetamide were added to the ground urea powder, followed by gentle mixing. The mixture undergoes the identical two-step heating procedure as that of the BCN synthesis process. The obtained products are denoted as EAy (y represents the amount of acetamide added), with the best performance referred to as EACN.

Supplementary Text S2. Materials Characterization.

The morphology of the samples was examined using a Scanning Electron Microscope (SEM, Tescan Mira LMS) operated at a 5.0 kV scanning voltage, as well as a Transmission Electron Microscope (TEM, FEI Talos F200X) with a 200 kV scanning voltage. The pore size distribution and specific surface area were characterized through nitrogen adsorption-desorption isotherms, performed on a Micromeritics ASAP 2460 instrument after degassing at 300 °C. Crystal structures were elucidated by X-ray diffraction (XRD) using a Rigaku SmartLab SE with a scanning rate of 5° per minute. The presence of functional groups was identified with a Fourier Transform Infrared Spectrometer (FTIR, Thermo Scientific Nicolet iS20). Solid-state Nuclear Magnetic Resonance (NMR) on a Bruker 400 M was employed to reveal the chemical interactions within the samples. The chemical state of the samples was analyzed using X-ray Photoelectron Spectroscopy (XPS, Thermo Scientific ESCALAB 250Xi). The adsorption of CO_2 on the catalysts was studied through Temperature Programmed Desorption (TPD, Mak 2920). The light absorbance properties were evaluated using UV-Vis diffuse reflectance spectroscopy on a Shimadzu UV-3600 Plus. Photoluminescence (PL) spectra and time-resolved transient photoluminescence (TRPL) measurements were obtained with a fluorescence spectrometer (Hitachi F-7000). The identification of reactive species was accomplished using Electron Spin Resonance (ESR) spectroscopy on a Bruker instrument. ^{31}P Solid State Nuclear Magnetic Resonance (NMR) was conducted on a Bruker Avance Neo 400 WB to further investigate the samples' properties.

Supplementary Text S3. Photocatalytic activities for CO_2 conversion.

For batch reaction, 10 mg catalyst and 5 mL of deionized water were introduced into a quartz reaction plate and thoroughly dispersed using ultrasound for a duration of 30 minutes. Subsequently, the mixture was transferred to an oven set at 60 ℃ to facilitate film drying, ensuring uniform adhesion onto the surface of the quartz reaction tray. Following this step, 200 microliters of deionized water droplets were added to the reaction tray which was then placed inside the reactor of batch reaction system (Fig. S12a). The reactor underwent vacuuming followed by multiple injections of CO_2 in order to eliminate any residual air within it. Once completed, the CO_2 pressure within the reactor was adjusted to reach 70 Kpa. Utilizing a xenon lamp with an intensity of 300 W and employing a 400 nm end filter as a light source, the lamp was activated to initiate the reaction process. Finally, product analysis was conducted using Foley 9790 chromatography.

To evaluate the catalytic activity and stability of the catalyst over an extended timescale, photocatalytic CO_2 reduction tests were conducted in a continuous flow reactor (Harrick reactor, Fig. S12b). Approximately 2 mg of NPEA photocatalyst was placed in the Harrick reactor, and a gas mixture of 1% CO_2 in argon balance was introduced into the reactor at a flow rate of 10 ml min^{-1}. The gas was humidified with deionized water before entering the reaction chamber to provide the necessary H_2O for the reaction. A 300 W xenon lamp was used as the light source to drive the reaction. The composition of the effluent was monitored using an online gas chromatograph (TRACE 1310, Thermo Scientific).

Supplementary Text S4. Electrochemical measurements.

The electrochemical measurements were conducted using a conventional three-electrode system, wherein the prepared thin film electrode served as the working electrode, a platinum plate (99.9%) was employed as the counter electrode, and an Ag/AgCl reference electrode was utilized. A 0.2 M Na_2SO_4 solution was employed as the electrolyte for these experiments. The photoelectrochemical characterization was performed using the CHI 660D workstation, with all experiments being carried out at room temperature.

Supplementary Text S5. Transient absorption spectroscopy (TAS).

The transient absorption spectroscopy of the samples was performed using an American ultrafast system, Helios. The output pulse was split into two beams: one beam was utilized for generating 350 nm laser pulses through second harmonic generation in a nonlinear optical crystal, serving as the excitation pulses; while the other beam with lower energy was focused onto a CaF2 plate (4 mm thickness) to generate a white light continuum acting as the probe. The time delay between the pump beam and probe pulses was controlled by a motorized delay stage. The transmitted probe light after passing through the sample was collected using a laser frequency-synchronized fiber optic spectrometer. By modulating the pump laser beam at half of its frequency (1 kHz), both on/off states were acquired for the probe light, enabling calculation of the pump pulse-induced optical density change in the sample. The samples were uniformly dispersed in water after 2 h ultrasound.

Supplementary Text S6. DFT calculation

The first-principle calculations were performed using the Density Functional Theory (DFT) within the Vienna ab initio simulation package (VASP). Molecular structural optimization was achieved through the Projected Augmented Wave (PAW) method with the Generalized Gradient Approximation (GGA), employing a 275 eV energy cutoff. A vacuum layer exceeding 15 Å was maintained to ensure a clear separation between periodic images. The convergence criterion for the residual forces on each atom was set to be less than 0.02 eV $Å^{-1}$, ensuring a high level of precision in the optimization process.

The time-varying density functional theory (TDDFT) simulation method was conducted to explore the electron excitation process. TDDFT calculations were performed using the Gaussian 09 software, employing B3LYP/6-311G/6-311G level of theory, followed by geometric optimization of the structure with VASP. Most of the structure and contour maps are realized through the visualization software VMD.

The free energy change (ΔG) for adsorptions was determined as follows:

$$\Delta G = (E_{total} - E_{slab} - E_{mol}) + \Delta E_{ZPE} - T\Delta S$$

Where E_{total} is the total energy for the adsorption state, E_{slab} is the energy of the pure surface, E_{mol} is the energy of the adsorption substrate, ΔE_{ZPE} is the zero-point energy change and ΔS is the entropy change.

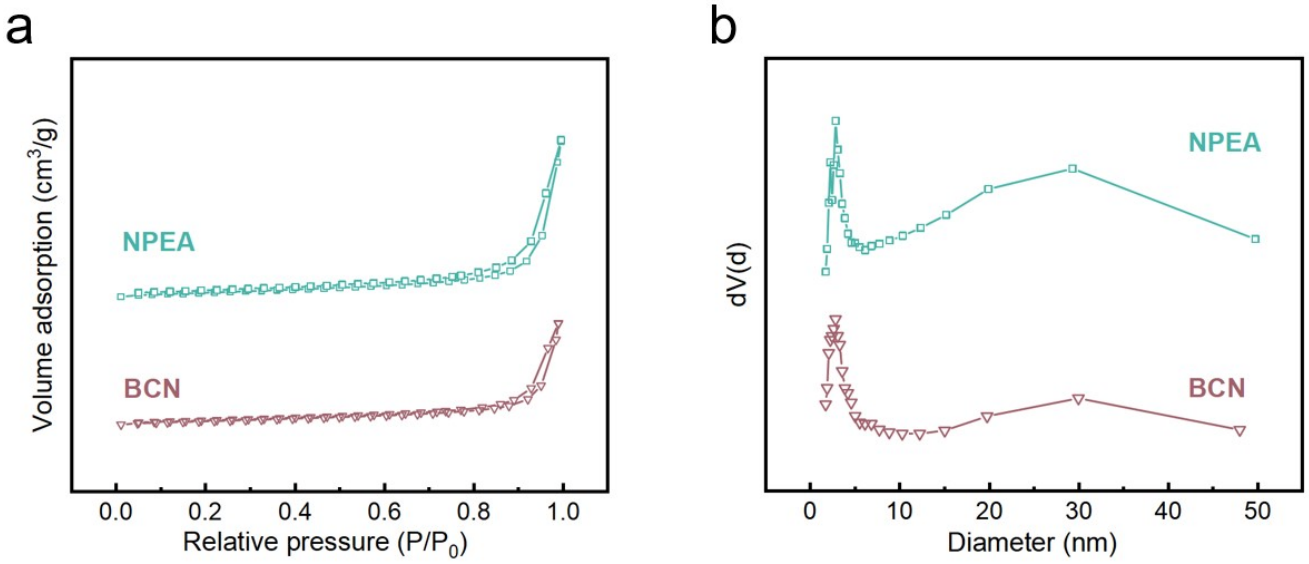

Fig. S1. (a) N_2 adsorption-desorption isotherms of BCN and NPEA. (b) Pore radius information of BCN and NPEA.

Due to its smooth and flat structure, BCN exhibits a relatively small specific surface area of 41.08 m^2/g and pore volume of 0.20 cm^3/g. Notably, NPEA shows remarkable enhancements in both specific surface area (51.71 m^2/g) and pore volume (0.30 cm^3/g) compared to BCN. The increase in specific surface area of NPEA can be attributed primarily to the structural fragmentation of the material and the introduction of methyl-induced in-plane defects. In addition, the enhanced pore volume can be attributed to the construction of the porous reaction chamber. The increased surface area and pore volume provide evidence for the favorable interaction between the methyl group and phosphorus atom within the carbon nitride morphology and structure.

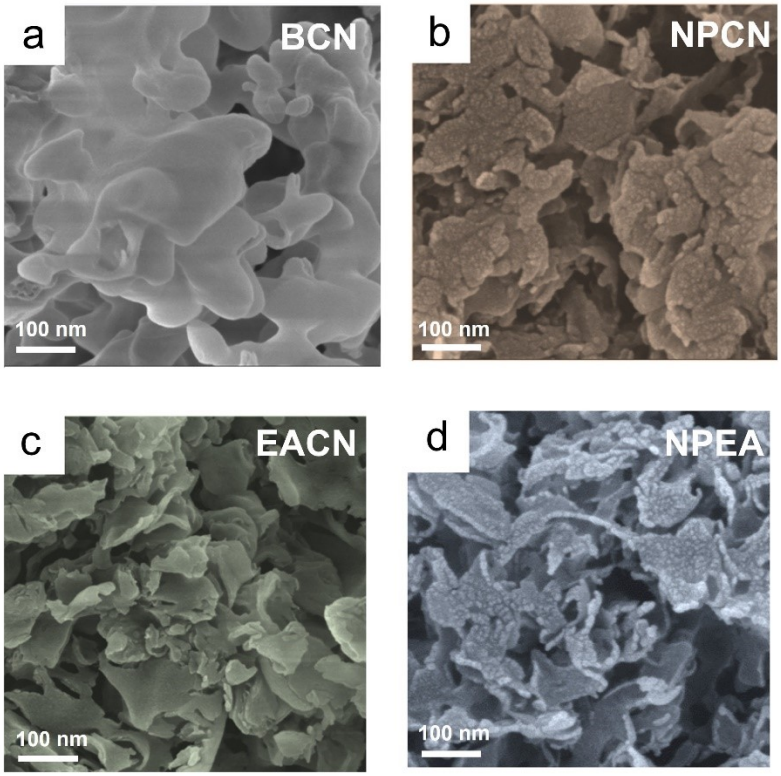

Fig. S2. The SEM images of the (a) BCN, (b) NPCN, (c) EACN, (d) NPEA.

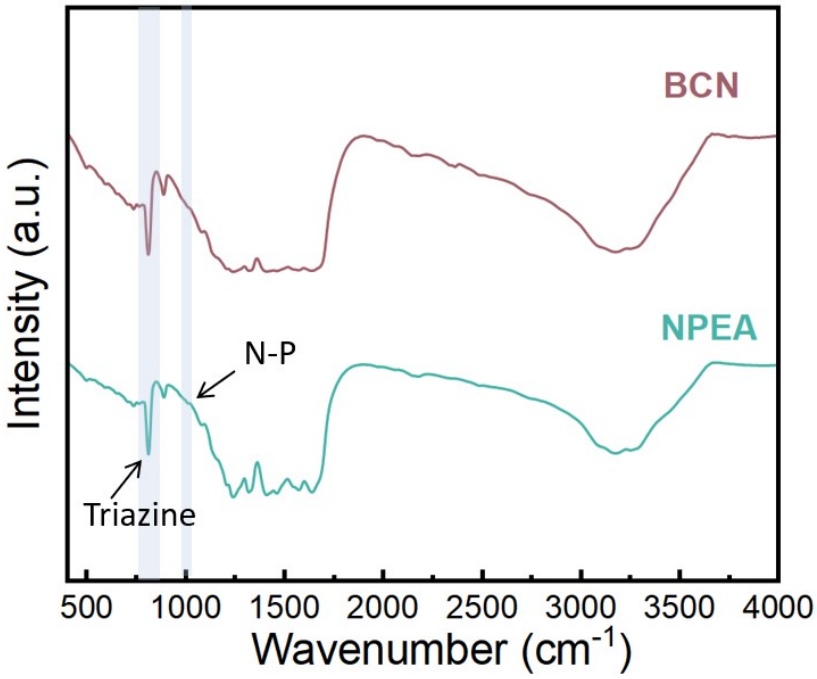

Fig. S3. The FT-IR spectra of BCN and NPEA.

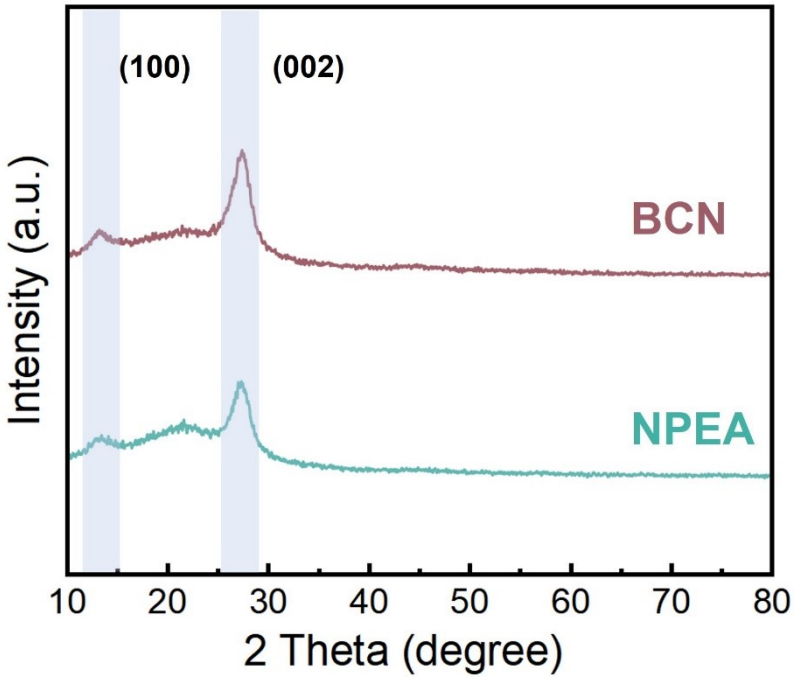

Fig. S4. The XRD spectra of BCN and NPEA.

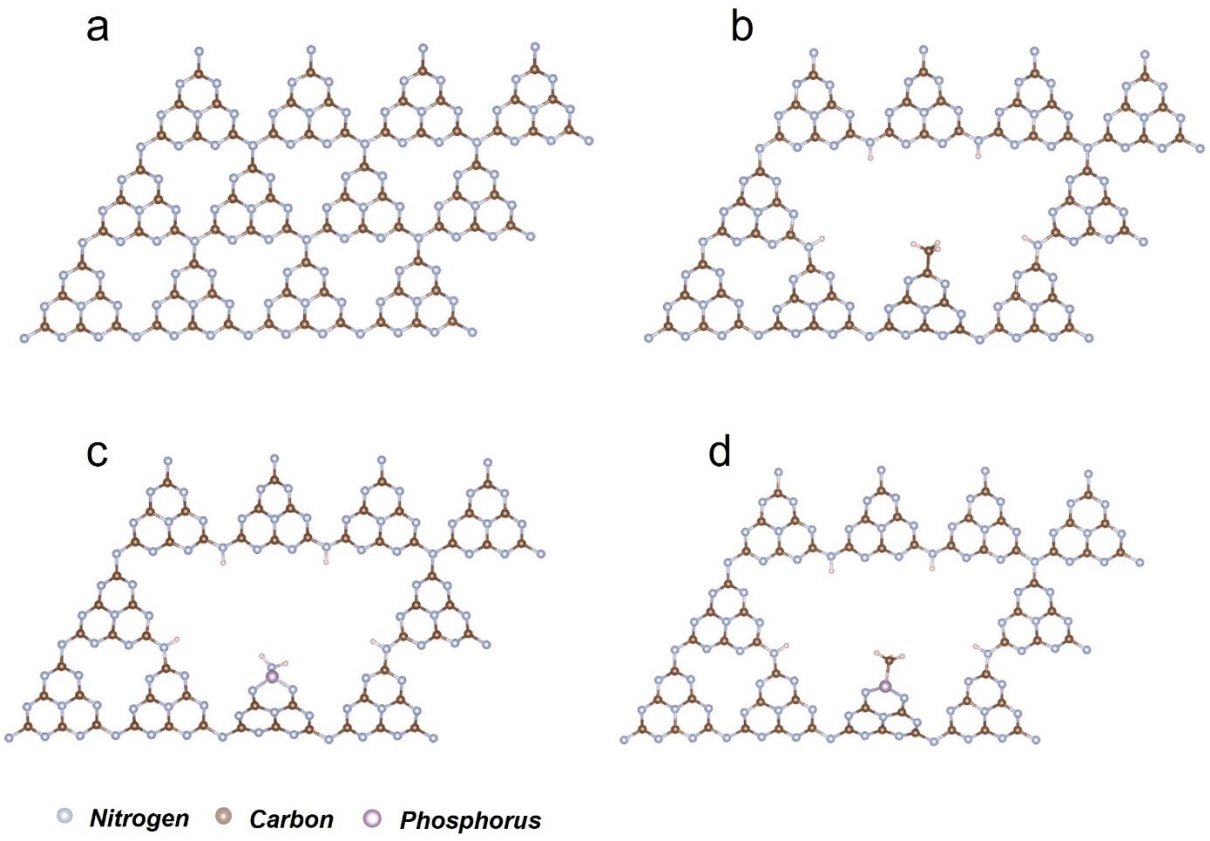

Fig. S5. Top view of the relaxed structure of established models for catalysts; (a) BCN, (b) EACN, (c) NPCN, (d) NPEA.

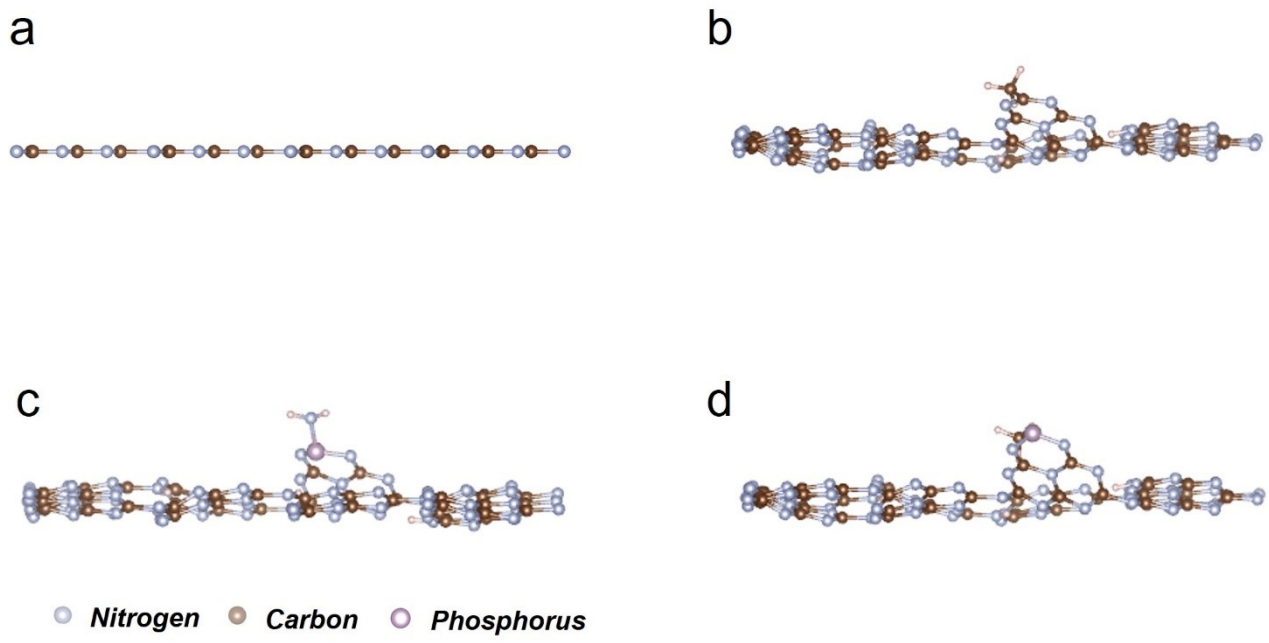

Fig. S6. Side view of the relaxed structure of established models for catalysts; (a) BCN, (b) EACN, (c) NPCN, (d) NPEA.

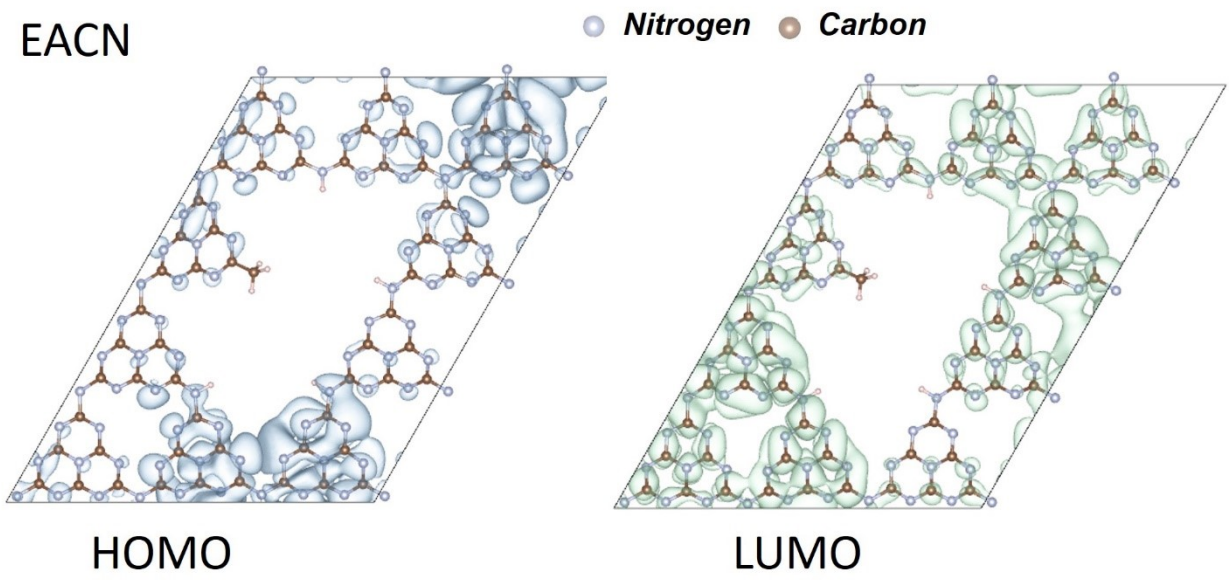

Fig. S7. The electronic structure of EACN with corresponding charge distribution of HOMO and LUMO.

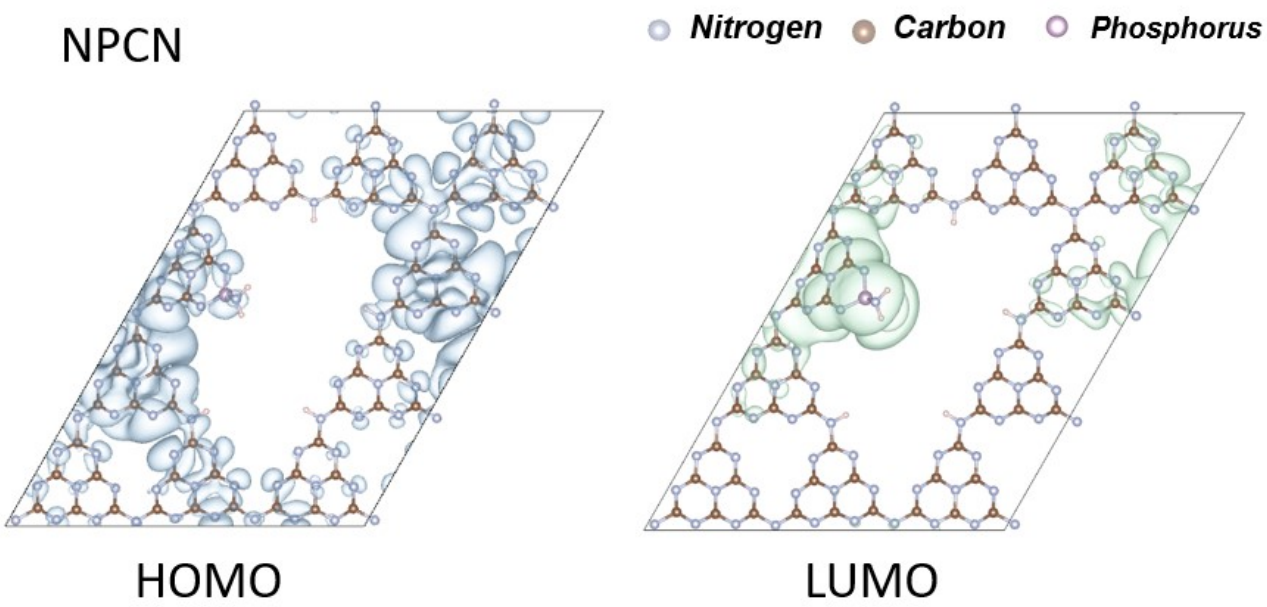

Fig. S8. The electronic structure of NPCN with corresponding charge distribution of HOMO and LUMO.

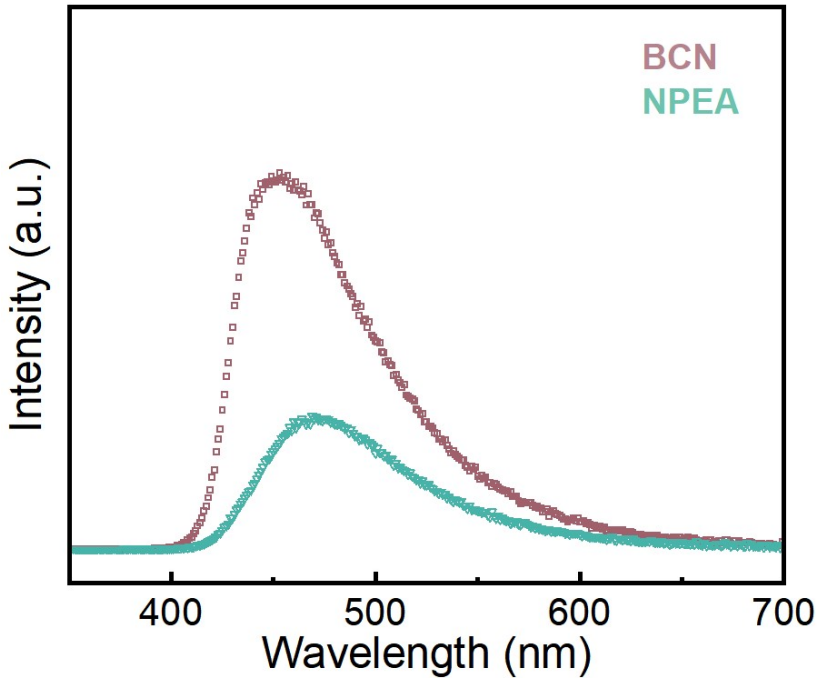

Fig. S9. The PL spectra of BCN and NPEA.

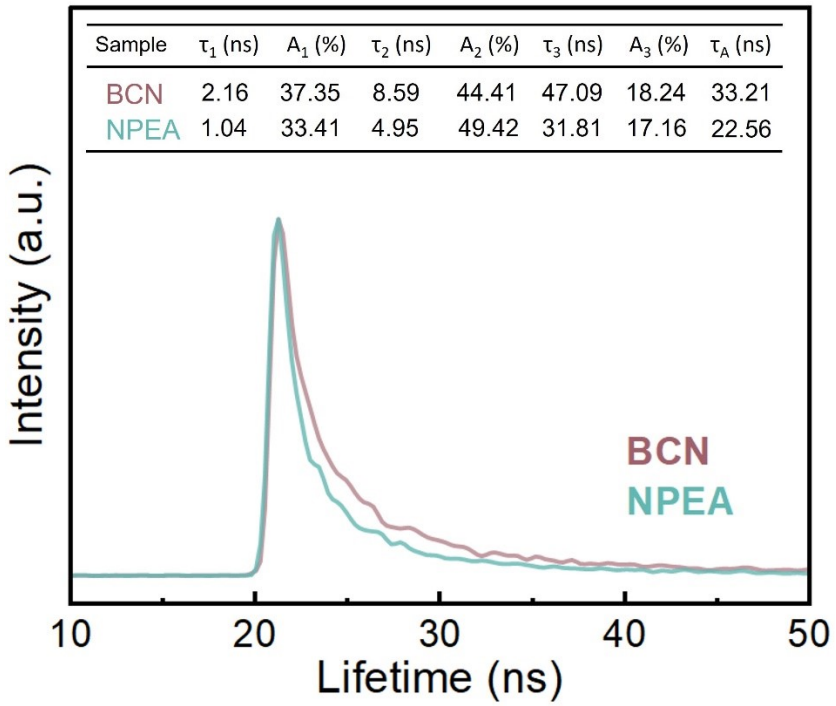

Fig. S10. The TRPL spectra of BCN and NPEA.

The TRPL decay curve of the sample was fitted using the followed exponential function. The average fluorescent lifetime (τ_A) of NPEA (22.56 ns) was significantly shorter than that of BCN (33.21 ns) due to the rapid radiation decay caused by the porous reaction chamber and the annular electron donor-acceptor structure.

$$I(t) = A_1\exp(-t/\tau_1) + A_2\exp(-t/\tau_2) + A_3\exp(-t/\tau_3)$$

$$\tau_A = \frac{A_1\tau_1^2 + A_2\tau_2^2 + A_3\tau_3^2}{A_1\tau_1 + A_2\tau_2 + A_3\tau_3}$$

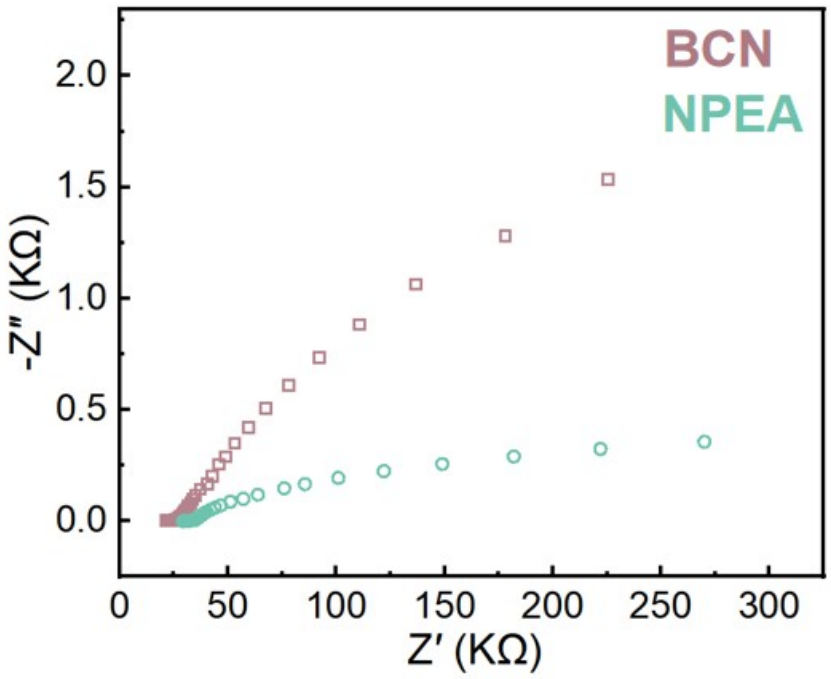

Fig. S11. The EIS Nyquist plots of BCN and NPEA.

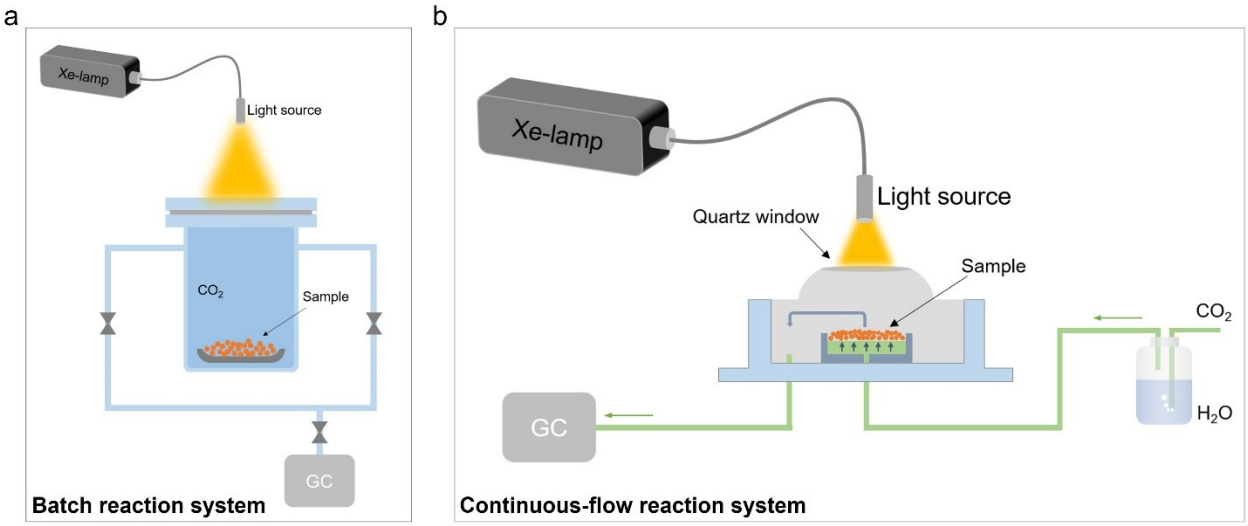

Fig. S12. Schematic diagrams of photocatalytic reaction system. (a) Batch reaction system. (b) Continuous-flow reaction system.

The Batch reaction system is utilized for conducting a single photocatalytic reaction. The Continuous-flow reaction system is utilized for conducting a long continuous photocatalytic reaction. The utilization of continuous flow reaction systems enables the implementation of long-term, uninterrupted photocatalytic reactions by employing a CO_2 cycle atmosphere and utilizing H_2O as the reaction feedstock.

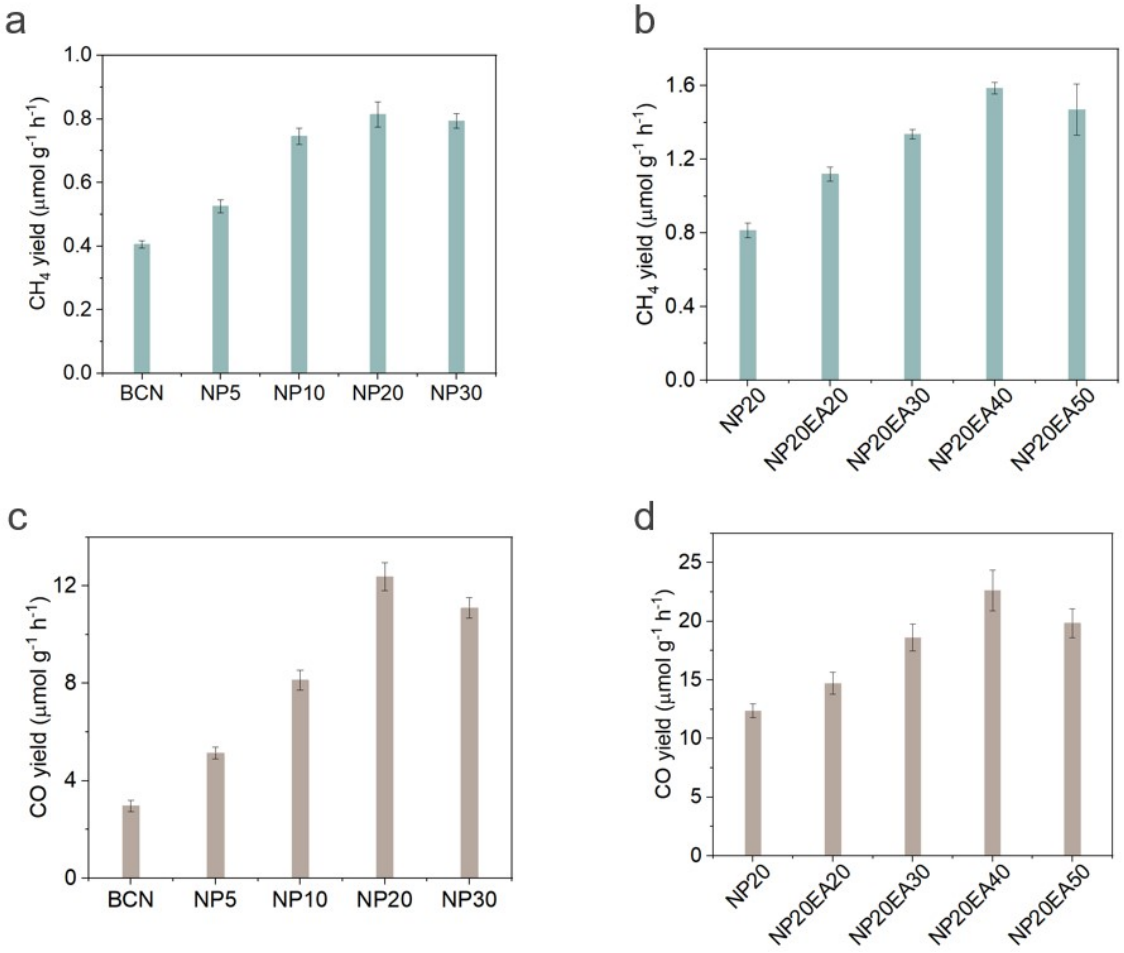

Fig. S13. Photocatalytic performance of different samples for CO_2 reduction to CH_4 (a-b) and CO (c-d) under visible light irradiation.

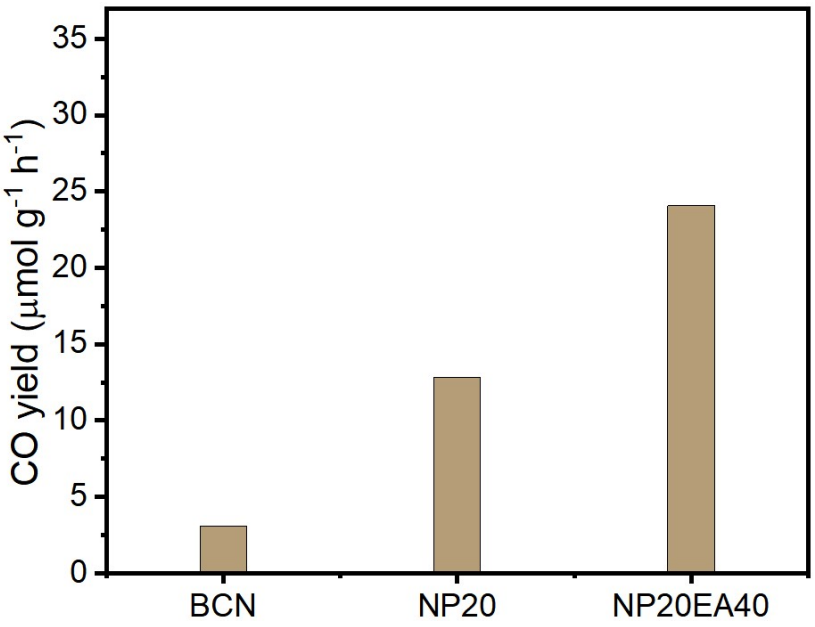

Fig. S14. The comparison of photocatalytic CO_2 reduction to CO among different samples.

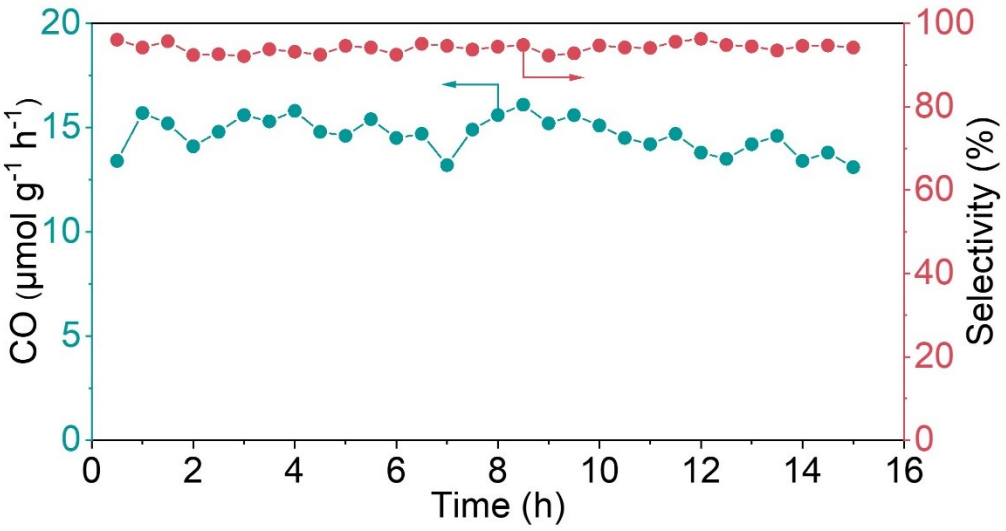

Fig. S15. The yield and selectivity of long-term photocatalytic reduction of CO_2 to CO by NPEA.

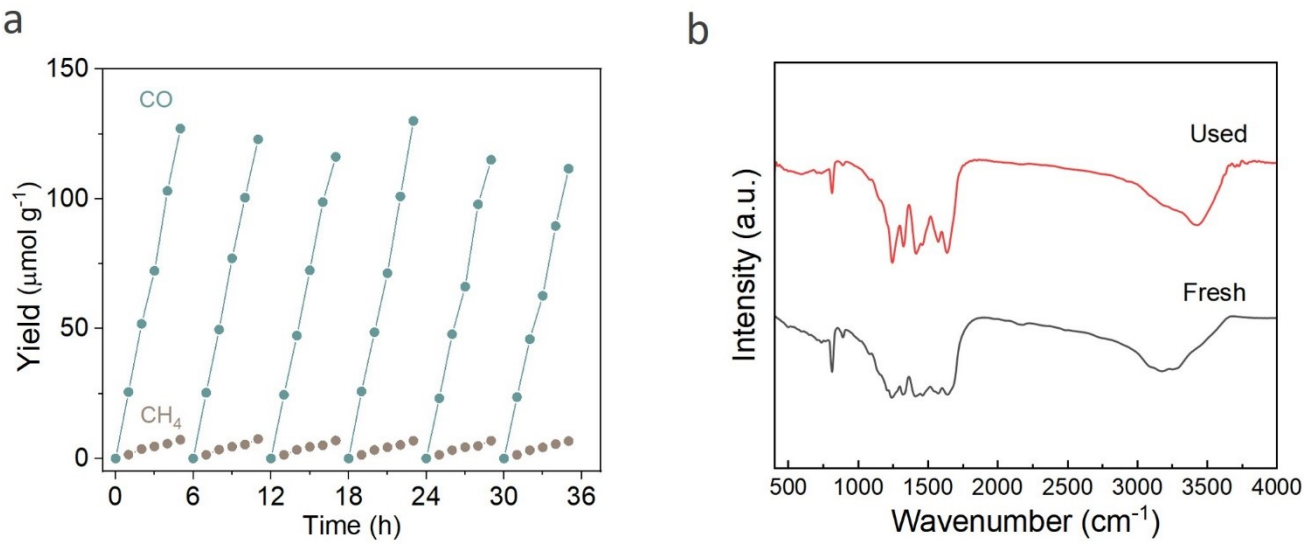

Fig. S16. (a) Photocatalytic performance of NPEA for long-term CO_2 reduction to CO and CH_4 over 5 cycles under visible irradiation. (b) FTIR spectra of fresh and used NPEA.

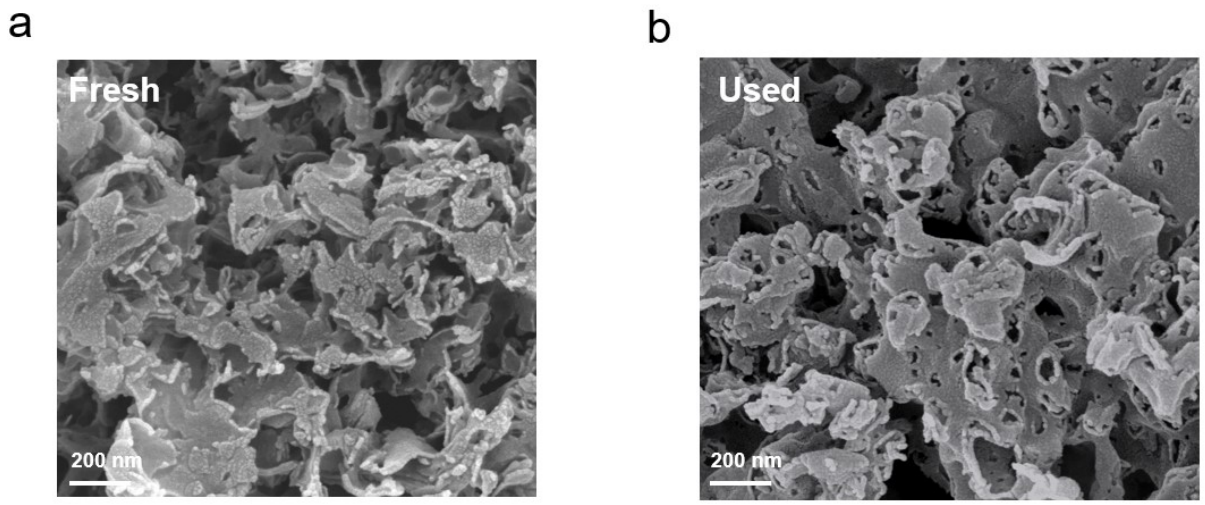

Fig. S17. SEM images of fresh (a) and used (b) NPEA.

It was obvious that NPEA after the 5-cycle long-term reaction still exhibits a granular surface and fragmented structure. Possibly attributed to the generation of gas (CO) during the reaction process, the edges of NPEA undergo a transformation into a curved morphology, accompanied by the emergence of numerous novel perforations.

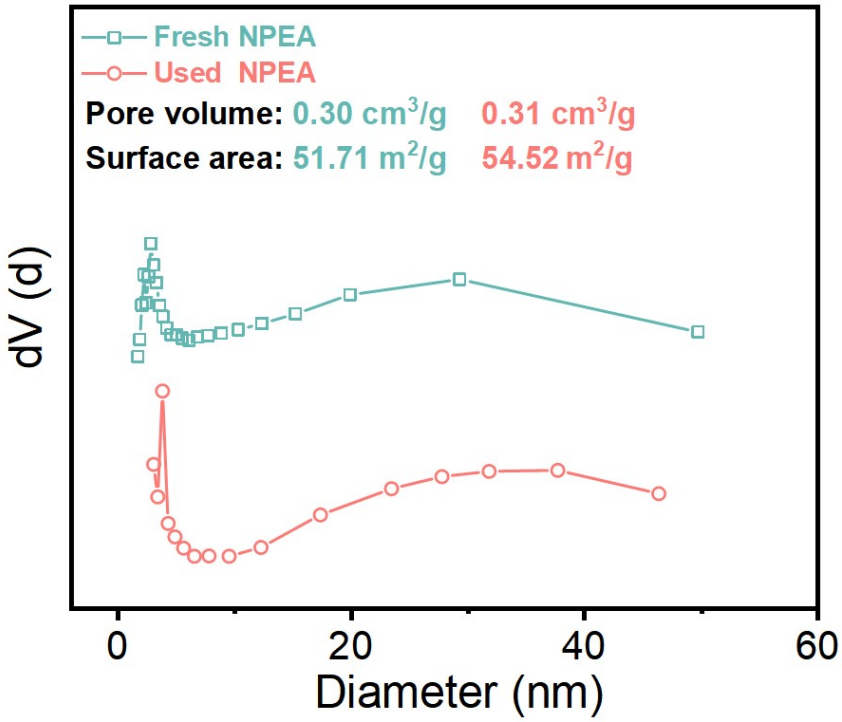

Fig. S18. Pore radius distribution information of fresh and used NPEA.

The variations in surface area and pore volume can be elucidated through the analysis of SEM images (Fig. S17, ESI†). The enhance in surface area may be attributed to the presence of curved edges on the NPEA after its usage. The increase in pore volume can be attributed to the emergence of new perforations.

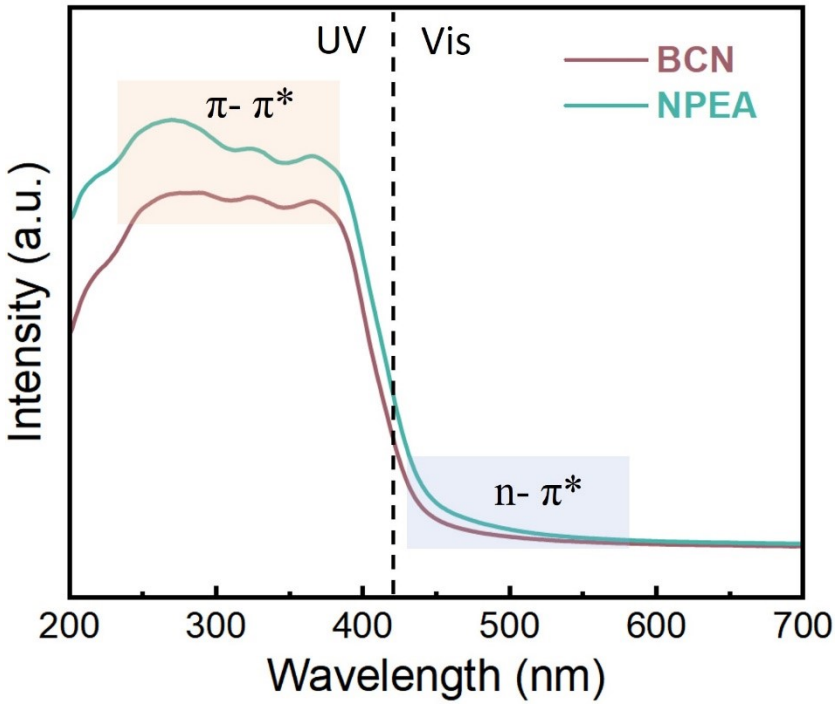

Fig. S19. The UV-Vis DRS spectra of BCN and NPEA.

The absorption spectra of all samples exhibit pronounced peaks in the 270~390 nm range, which can be attributed to the π-π* electron transitions. Notably, NPEA demonstrates significantly higher light absorption intensity compared to BCN within this region due to the unique electronic properties conferred by the phosphorus atom, thereby enhancing the π-π* electron transitions of the catalysts. Furthermore, NPEA exhibits slightly stronger absorption than BCN in the 450~550 nm range, indicating an enhancement of n-π* electron transitions facilitated by a fragmented structure induced by methyl group incorporation that disrupts the framework of the catalyst.

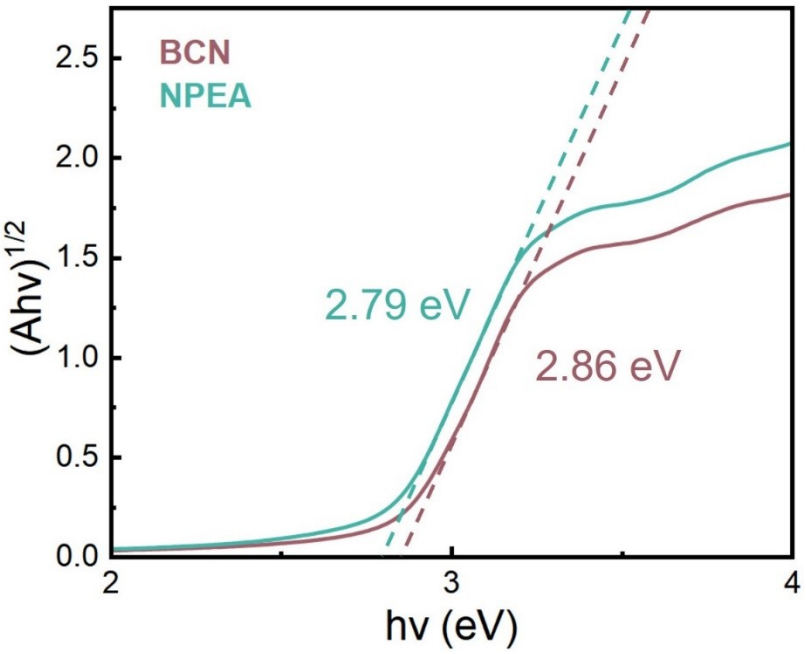

Fig. S20. The transformed Kubelka-Munk function of BCN and NPEA.

The band gap was determined by analyzing the Kubelka-Munk function data obtained from diffuse reflectance spectroscopy (DRS) data. In principle, photocatalysts exclusively utilize light with energy surpassing the energy threshold of band gap. Notably, NPEA (2.79 eV) exhibits a slight narrower band gap compared to BCN (2.86 eV), indicating an enhanced utilization of visible light for NPEA.

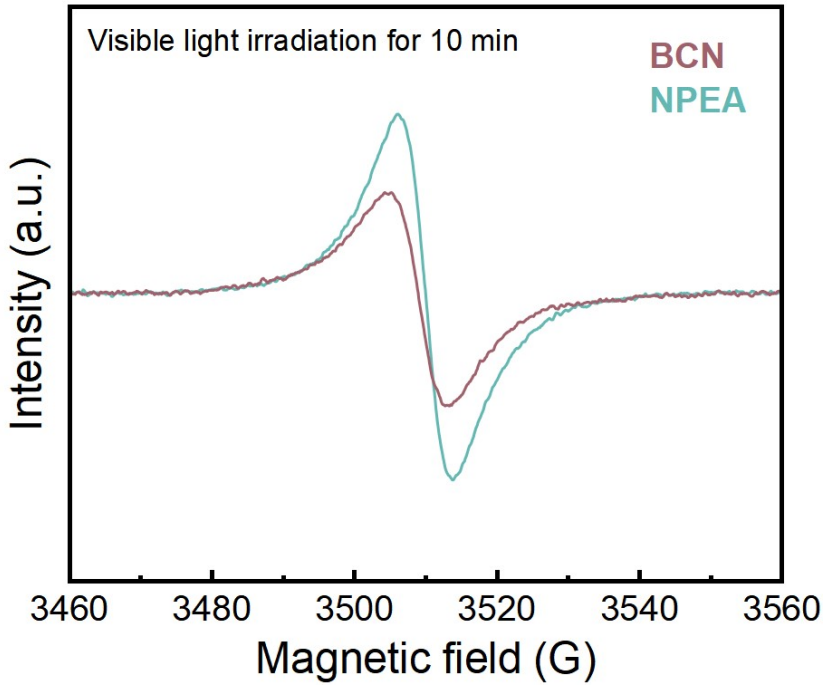

Fig. S21. The EPR spectra of BCN and NPEA under visible light irradiation.

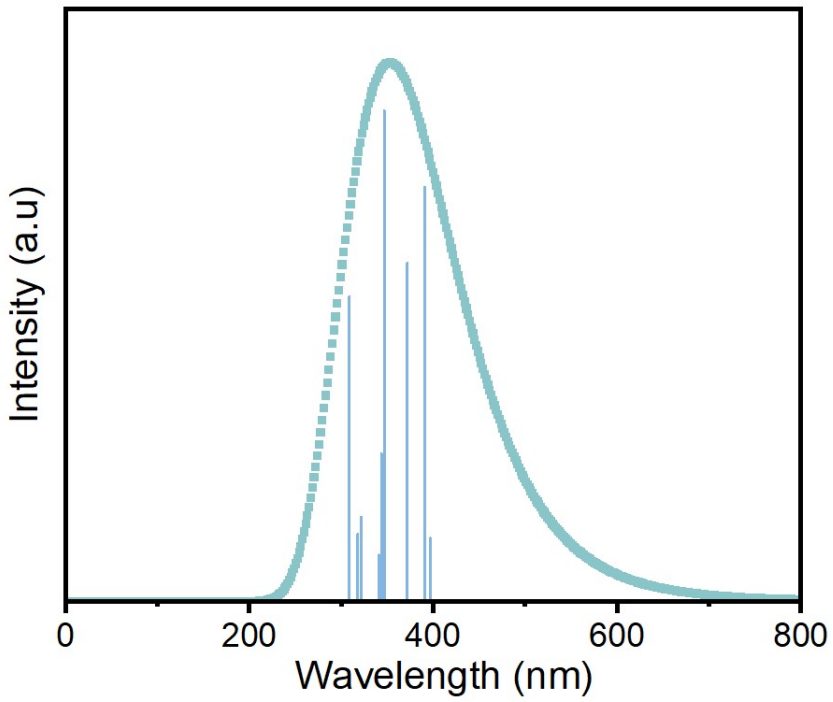

Fig. S22. The excited state absorption features of BCN obtained by time-dependent density functional theory calculation.

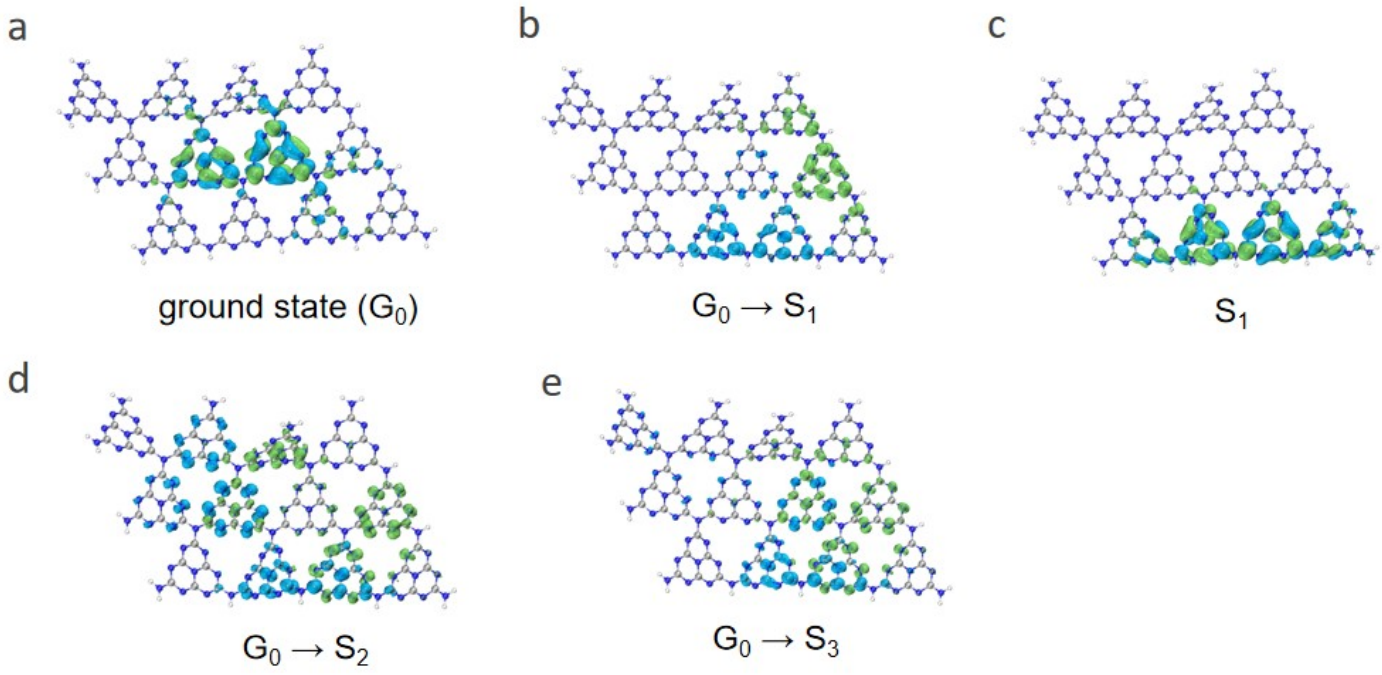

Fig. S23. The distributions of excited state with different energy levels and ground state of BCN.

The short life of positive features of BCN in TAS precisely corresponds to the rapid relaxing of excited-state absorption. The distributions of excited state with different energy levels and ground state of BCN were visualized by density functional theory (DFT) calculations (Fig. S19, ESI†). It was obvious that the distribution of the ground state and first excited state (S1) occurred within the same triazine ring, while the excited state of the higher energy level is separated from the ground state. The smooth surface and complete molecular structure of BCN can effectively facilitate the excited state electron transition to higher energy levels. After absorbing the pump light, BCN transitions to an excited state, followed by subsequent absorption of energy from the detection pulse and further transition to a higher excited state, thereby generating positive TAS features. As the fade of detection pulse energy, the electrons in the higher excited state of BCN continue to relax, resulting in feeble fluorescence emission that corresponds to the negative TAS features (Fig. 4b).

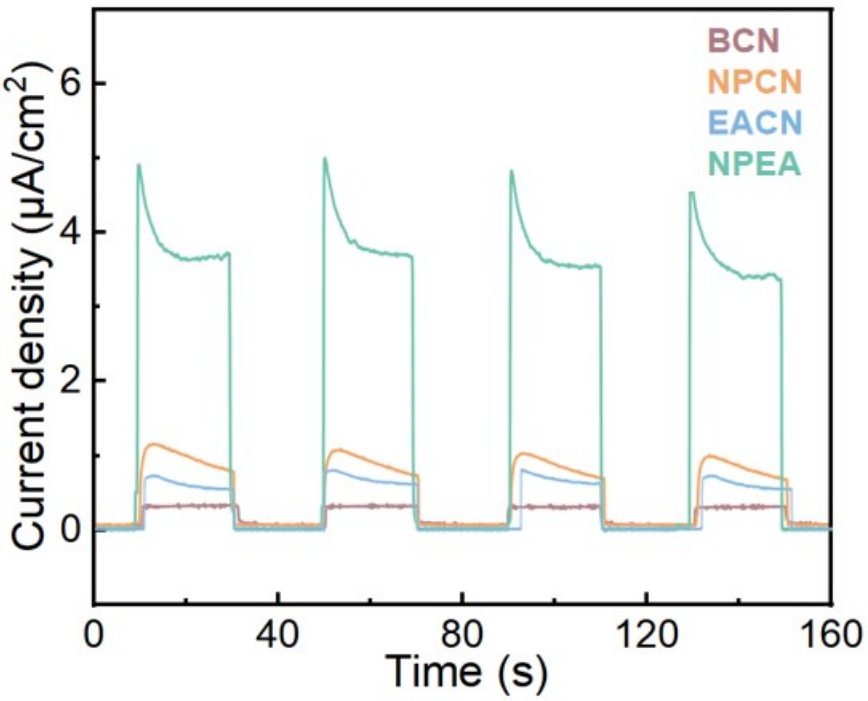

Fig. S24. The photocurrent response of the prepared samples.

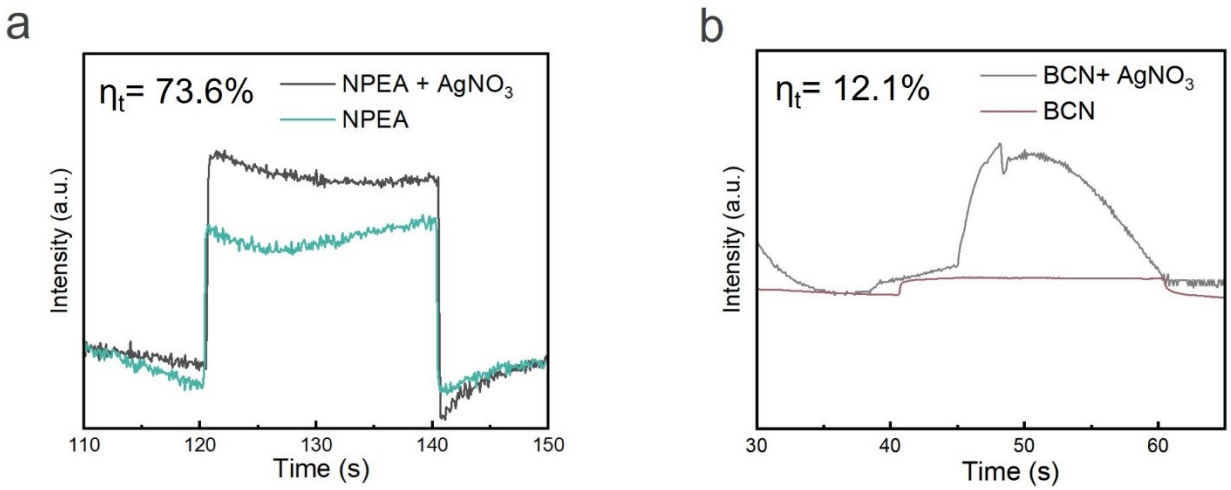

Fig. S25. The photocurrent density of NPEA (a) and BCN (b) under visible light irradiation without and with $AgNO_3$.

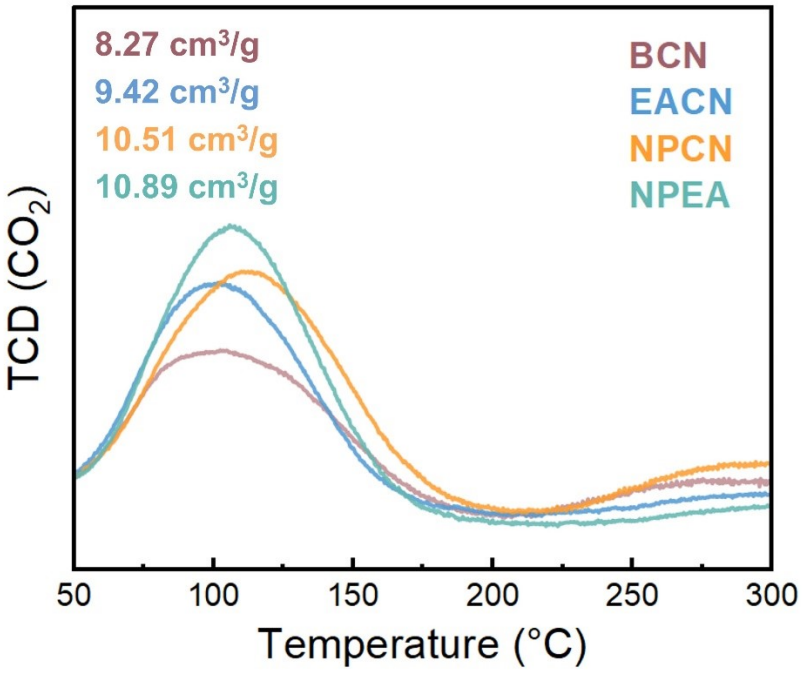

Fig. S26. Temperature programmed desorption of CO_2 with the prepared samples.

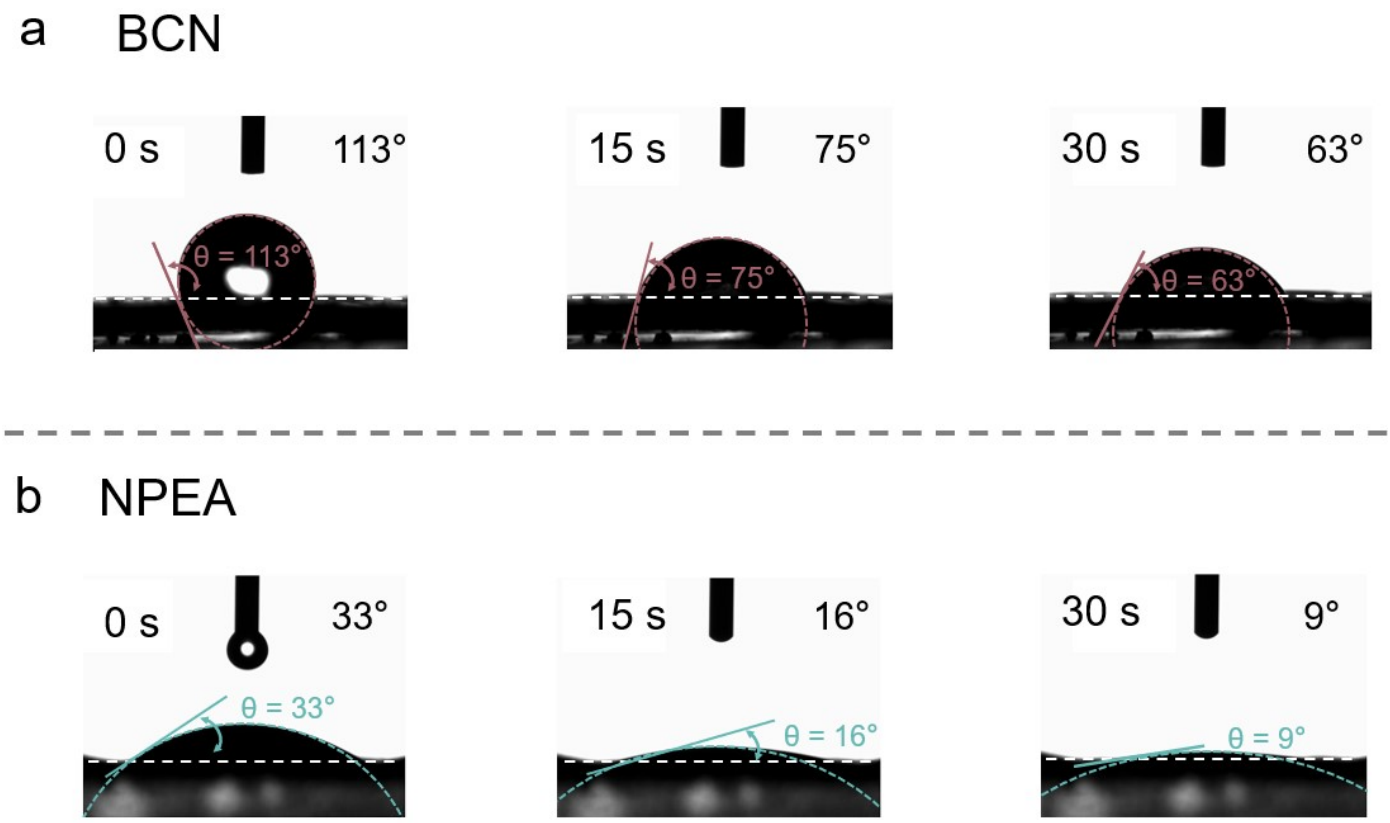

Fig. S27. The water contact angles (θ) of (a) BCN and (b) NPEA.

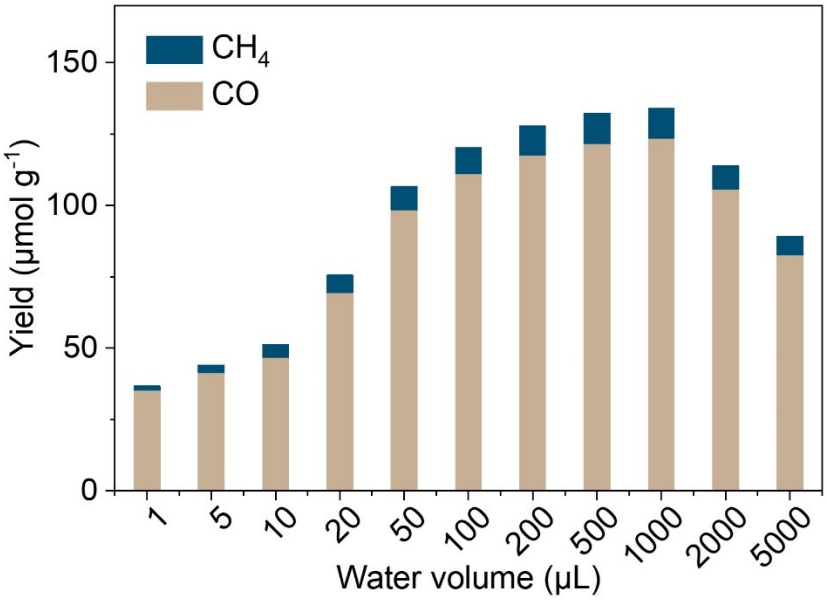

Fig. S28. The yield of CO and CH_4 for the photoreduction of CO_2 following a 5-hour reaction with different initial H_2O quantity.

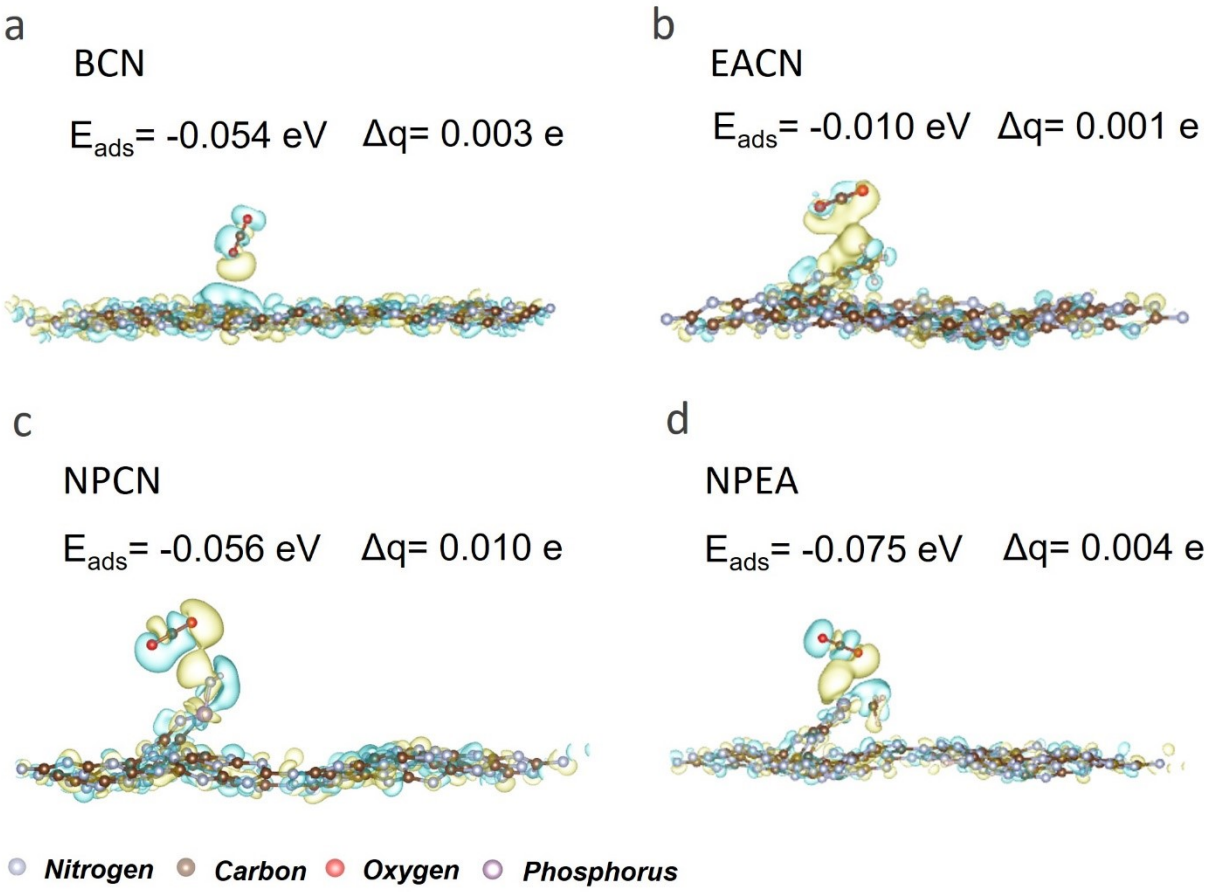

Fig. S29. The calculated absorption energy and charge transfer between catalyst and CO_2, and the corresponding visualization of adsorption behavior. (a) BCN, (b) EACN, (c) NPCN, and (d) NPEA.

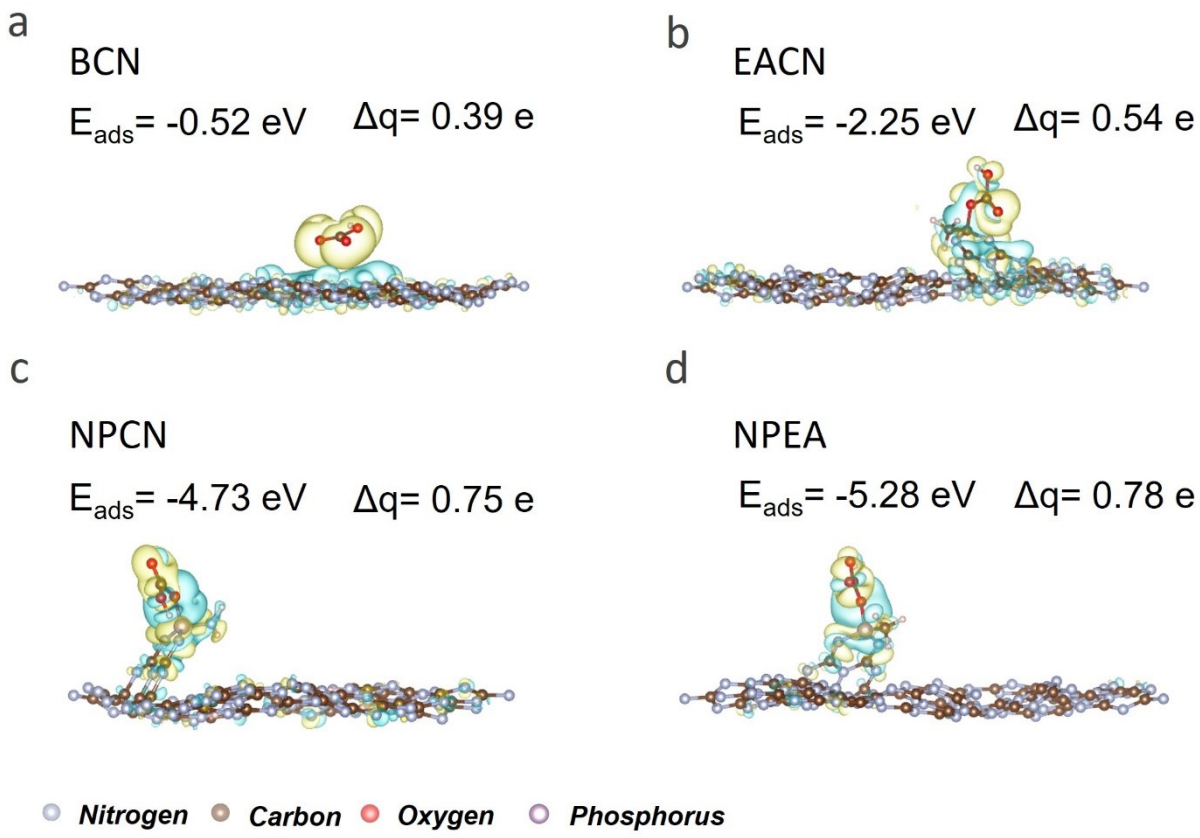

Fig. S30. The calculated absorption energy and charge transfer between catalyst and HCO_3^-, and the corresponding visualization of adsorption behavior. (a) BCN, (b) EACN, (c) NPCN, and (d) NPEA.

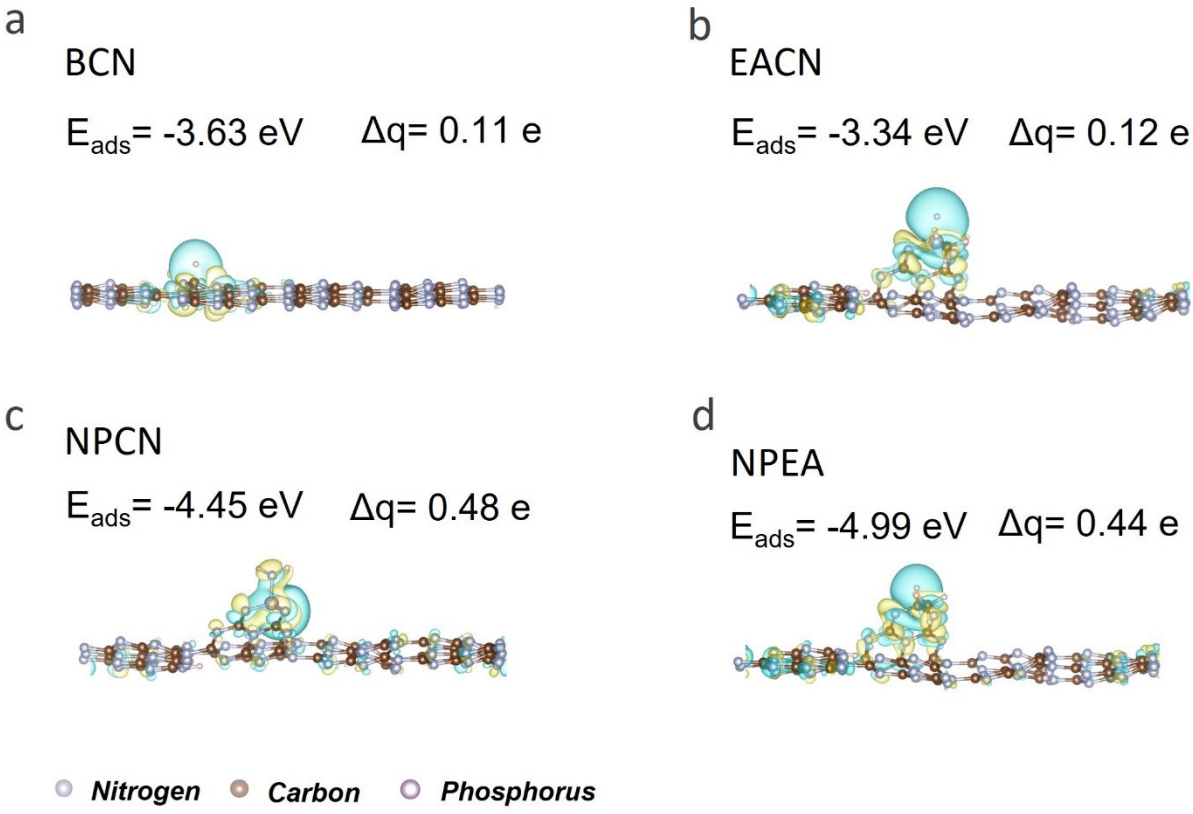

Fig. S31. The calculated absorption energy and charge transfer between catalyst and H^+, and the corresponding visualization of adsorption behavior. (a) BCN, (b) EACN, (c) NPCN, and (d) NPEA.

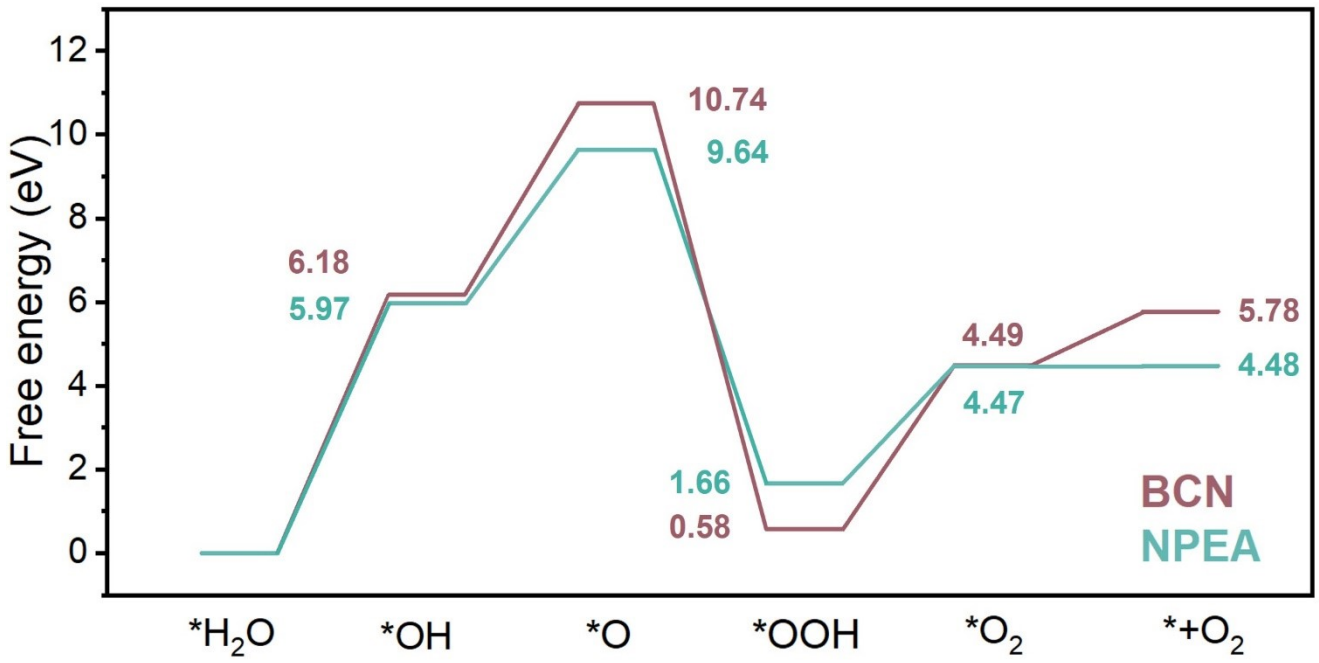

Fig. S32. Gibbs free energy diagrams for the intermediates formed during the oxidation of H_2O to O_2.

The more gradual variation in free energy observed in NPEA indicates a more favorable H_2O oxidation process on NPEA.

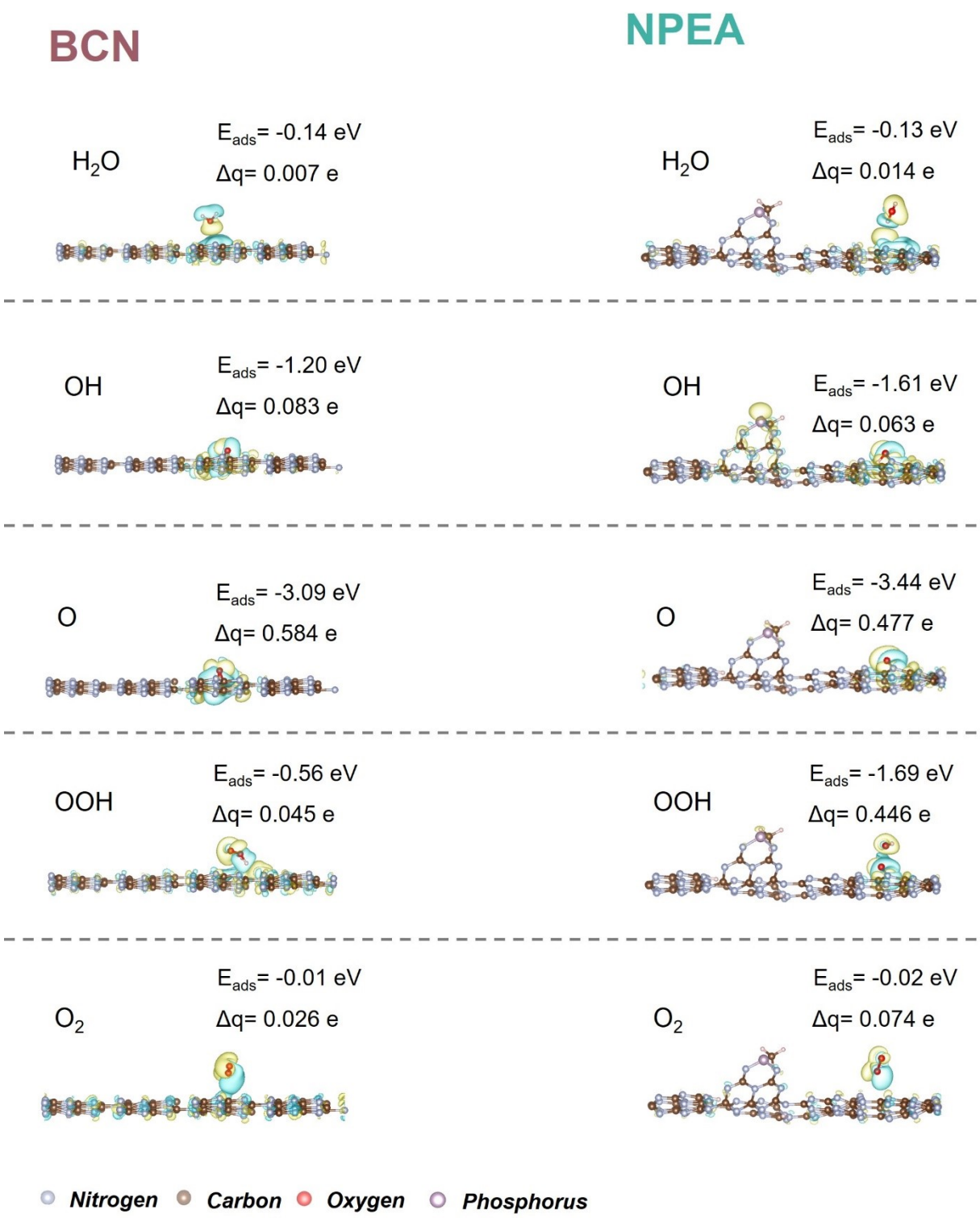

Fig. S33. Adsorption energy and charge transfer between intermediates and catalysts in H_2O oxidation reaction.

The key intermediates (OOH) in the process of H_2O oxidation exhibited enhanced adsorption energy and charge transfer on NPEA, indicating its heightened reactivity towards H_2O oxidation.

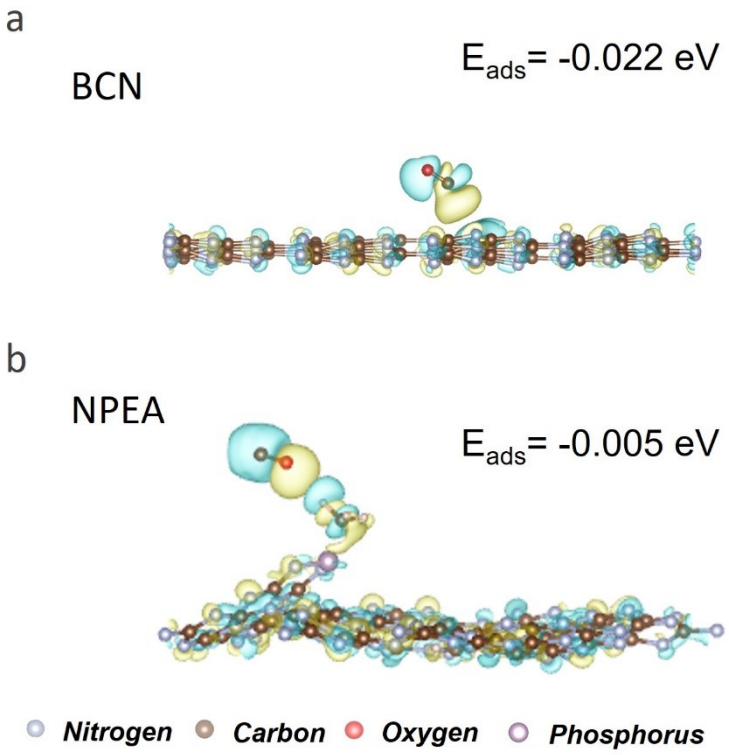

Fig. S34. The calculated absorption energy and charge transfer between catalyst and CO, and the corresponding visualization of adsorption behavior. (a) BCN, (b) NPEA.

Table S1. The specific surface area and pore structure information of samples.

Sample	BET surface area	pore volume
BCN	41.08 m^2/g	0.20 cm^3/g
NPEA	51.71 m^2/g	0.30 cm^3/g